



Application of CNN-BP on Inconel-718 chip feature and the influence on tool life

Shao-Hsien Chen¹ · Ming-Jie Zhang²

Received: 18 February 2022 / Accepted: 1 July 2022 / Published online: 23 July 2022
© The Author(s), under exclusive licence to Springer-Verlag London Ltd., part of Springer Nature 2022

Abstract

The hard-to-cut material nickel-base Inconel-718 is used in large quantities in the aerospace industry and defense industry because the Inconel-718 has good mechanical strength at high temperatures, but the tool is likely to wear in the cutting processes. In this study, chip color and features were employed to predict tool lives because the chips are the closest to the cutting tool in the shear zone during the cutting processes, which can more authentically reflect the phenomenon of tool wear. The changes in chip color and geometric shape were extracted and digitized, and the prediction method employed a two-stage model. In Stage 1, a convolutional neural network (CNN) was used for chip condition classification and validation, and in Stage 2, back propagation neural network (BP) was employed to predict the tool wear. The result showed that when the Google-Net and ResNet50 network models were adopted for CNN chip feature recognition, with the confusion matrix of multi-classification for validation, the recognition precisions were 66.7% and 88.9%, respectively. The modeling and prediction were performed in the BP neural network; the chip chromaticity, chip thickness, and chip width were employed as input features, and the precision was enhanced by multi-fusion features. Finally, the mean absolute percentage error values for heavy cutting were 17.11%, medium cutting at 5.45%, and small cutting at 9.02%, indicating that the CNN-BP prediction model has good forecast accuracy, thus providing a new model prediction form for tool life.

Keywords Inconel-718 · CNN-BP · Chip color · Tool wear

1 Introduction

The nickel alloy Inconel-718 has strengthened mechanical properties at high temperatures, and the strengthening mechanisms are γ' phase and γ'' phase precipitation strengthening, grain boundary strengthening, solid solution strengthening, precipitation hardening, and affiliation phenomenon, leading to rapid wear of cutting tools in the cutting processes. In this study, chip color and features were employed to predict tool lives. As the cutting tool is the closest to chips in the shear zone during the cutting processes, the tool wear can be reflected authentically [1]. This study discusses important issues, and the convolutional neural network (CNN) was adopted, as mentioned in earlier studies to determine

the wear of tools when cutting nickel alloy materials, which were fused with the studies about chip color, color correction, and material chips.

The nickel alloy Inconel 718 is characterized by high strength, lower thermal conductivity, and high work hardening at high temperatures, so the cutting force and tool wear increase with the radial depth of cut. Conventional cutting tools have problems of worse resistance to high temperature and abrasion performance. Thus, we tried a new cutter material, using a coated cutting tool with a special tool face to turn nickel alloy and found that the coated cutting tool had good repulsion to groove wear and tool flank wear [2–4]. The research conclusion showed that in the chip formation variation mechanism of nickel alloy Inconel 718, the serrated or segmented chip phenomenon was advisable for reducing the cutting force level, and that the chip formation mechanism of nickel alloy Inconel 718 was very important for effective and efficient machining from the analysis model [5, 6]. The tool wear characteristic in nickel alloy cutting with the characteristic of the general ferrous alloy and indicated that the cutting force was twice as high as

✉ Shao-Hsien Chen
e6036@ncut.edu.tw

¹ The Graduate Institute of Precision Manufacturing, National Chin-Yi University of Technology, Taichung, Taiwan

² Department of Mechanical Engineering, National Chin-Yi University of Technology, Taichung, Taiwan

that of general carbon steel in nickel alloy cutting at the same speed, so that the tooltip end bore super high stress and temperature, as the maximum cutting temperature was close to the cutting edge end, the maximum depth of crater wear was closer to the cutting edge end than ferrous alloy, and the tool flank wore severely due to high temperature of tool face, the tool life was shortened, and the cutting speed could not be increased [7].

Used CNN for borehole image recognition and divided the recognition criteria into three grades: red, yellow, and green, which corresponded to three stages of the drilling state. The red grade means a worn state of the drilling bit and should be changed immediately in the drilling process [8–10]. Using CNN model for automatic recognition of the wear type of high-temperature alloy cutting tool in the face milling process, used convolutional auto-encoder (CAE) to pretrain the network model and combined BP with stochastic gradient descent (SGD) algorithm for fine-tuning of model parameters [11, 12]. The deep learning method indirectly identifies the tool wear level based on the image processing for turning chips. Different features are extracted from RGB and HSV (hue, saturation, value) image channels, and the neural network is set up according to the tool wear state condition to classify the chips [13].

The vibration monitoring method is generally implemented by mutual extrusion of machine cutting tool and workpiece, so the reciprocity is very high. The state of the vibration frequency of the cutting tool is changed as the tool is worn and damaged, so the vibration monitoring method usually places the sensors nearby the cutting edge of the cutter; the vibration signals are captured and combined with the charge amplifier to analyze the collected values; the required feature values are selected for monitoring. The method is reliable to some extent, but the vibrational state of the cutting tool and the interference of the external environment should be removed to some extent, to extract the required data effectively [14, 15].

A vibration sensor was combined with an artificial neural network for the classification of cutting tool conditions and acceleration data training. The monitoring aims to optimize vibration signals and performs artificial neural network operations to obtain various precisions and indicates the performance of cutting tool conditions. The collected time-series and milling vibration signals of workpieces are different, and the exact values are obtained by various neural network analyses [16, 17].

Kamdani [2] used multiple machining paths to monitor the machining process of fine milling, the load current in various axial directions and the spindle vibration signals could be collected effectively and instantly, and the automatic segmentation method of signal data was further

improved to enhance the noise reduction capability and shorten the data analysis time. The experimental results showed that the wavelet was used for noise processing, and the S/N ratio of the five-level db3 generating function was increased from 11 dB before denoising to 15.63 dB. In terms of the accuracy of characteristic set prediction, the mean absolute percentage error (MAPE) rates of inner circle roundness, inner circle cylindricity, and outer circle roundness were estimated to be 8.65%, 13.2%, and 6.5%, applicable to fine milling to predict the machining accuracy [18].

In this study, the current signal characteristic in the machining was used as a monitoring method to analyze the state of tool wear. In analysis feature selection, the cutting load current signals of different paths were collected and converted into time–frequency domain signals; the data were classified by Markov state and K-means clustering, the required feature values were selected, and according to the test results, the classification accuracy was 74.61 ~ 91.62%; the average recognition was 83.39% [19, 20].

The visual inspection method for images generally uses optical inspection or a vision processing system to judge the extent of the damage. The method measures the damage condition of the main body of workpiece material according to the optical position of the image acquisition unit to evaluate the worn surface. It has the advantage of capturing optical measured values (e.g., actual geometry change induced by wear). Optical measurement is a difficult technology for machining because the tools should be dismantled frequently for measurement. Besides the above measuring method, an automatic solution based on calculator vision was worked out recently for identifying the damaged insert in the edge contour milling head. Upon the completion of this experiment, very high accuracy was obtained; the method can facilitate online measurement of the defects, thus making it another cutting tool monitoring method [21, 22].

In this study, the tool life, tool wear, and image acquisition and the degree of wear of the cutting tool profile were analyzed. The experimental results showed that a tool wear measurement system of in situ machine vision was built, and the edge contour could be established for the tool edge at the front end of the milling cutter. Next, the wear width and height of the milling cutter were drawn and analyzed, the subtle changes in the two values were analyzed, and the measurement result was obtained [23].

The objectives of this study include (1) evaluating and calibrating the effectiveness of charge coupled device (CCD) chromaticity; (2) comparing different prediction methodologies, processes, and measurement signals on the relationship between chip color and tool wear; and (3) investigating the influence of chip color and geometric shape on tool wear.

2 Cutting principle and prediction method

2.1 Tool life and principle

The tool life in the cutting processes is defined as the result of physical action and chemical action resulting from cutting heat and mechanical friction during cutting. The tool wear appears as the wear band, gap, and fracture on the back of the cutting tool; the relationship between tool life and cutting speed is the tool life criteria proposed by F.W. Taylor in 1894, and expressed as Eq. (1); the relationships of different types of materials are shown in Fig. 1 [24, 25].

$$VT^n = C \tag{1}$$

When the influence of feed rate and the depth of cut on tool life is considered in the cutting processes, the tool life criterion is expressed as Eq. XX, so the cutting speed, feed rate, and depth of cut are variable factors, and different workpieces, cutter materials, tool angle forms, and coatings can influence the constants of n and C .

$$VT^n f^{n1} d^{n2} = C \tag{2}$$

$n, n1, n2$: constants depending upon tool material ($= 0.1$ to 0.4); C : constant that depends on tool-work material combination and tool geometry (> 100); V : cutting speed (m/min), T : tool life (min); C : empirical constant; n : constant of cutter material properties.

According to the tool life curve, the major influencing factors include the coordination of cutter material and workpiece material, cutting speed, cutting thickness, and cutting width. In metal processing, the time of processing shortens as the cutting speed increases, with better processing surface accuracy, but the wear rate of the cutting tool increases, meaning the tool life is shortened. The two forms of wear are (1) tool face wear resulting from the crater when the chips flow through the tool face and (2) tool flank wear region induced by rubbing action of the fresh working surface.

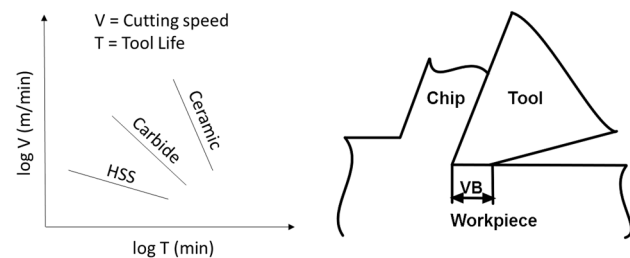


Fig. 1 Relationship between tool life and cutting speed

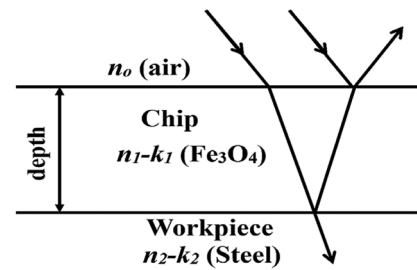


Fig. 2 Oxidation film model

2.2 Chip chromaticity measurement and transformation

In this study, a measuring equipment and method for chip color of machining chip features were developed, to predict the tool life using chip features, to reduce errors, and to increase the machining precision. In the cutting of metal materials, the high-speed friction between cutting tools and workpiece materials generates a lot of cutting heat, and the chips are heated up rapidly by the cutting heat. As the chips cut off the parent material and cooled rapidly in the air, this phenomenon results in oxidation films of different colors on the surface of chips. The color of the oxidation film is influenced by the thickness of the oxidation film (d), refractive index (n), and absorption coefficient (k) of the oxidation film and parent material, as shown in Fig. 2. The color of chips during machining changes in the order of from light olive gray (2.5Y) pale brown (2.5Y) weak brown (5YR) dusky purple (10P) dusky bluish purple (10 PB) moderate blue (2.5 PB) weak blue (10B) medium bluish-gray (5G) light olive-gray (7.5GY) weak red (5R) [26].

Figure 3 shows the relation between chip oxidation film thickness and chromaticity coordinate points, and the

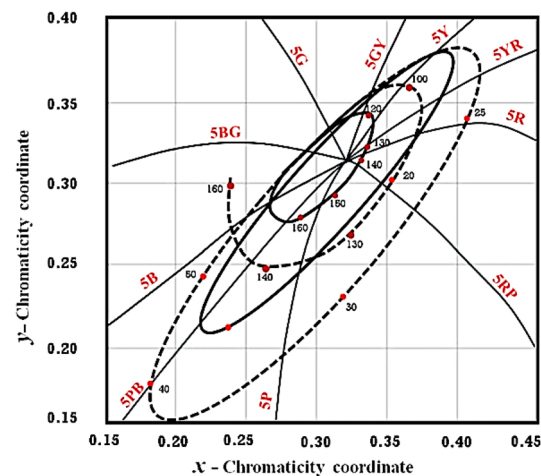


Fig. 3 Chromaticity diagram [26]

relation graph shows annular solid lines. The lines radiating from the center represent yellow (Y), red (R), purple (P), blue (B), and green (G) hues. Oxidation film thickness (μm), chromaticity coordinates (x_c, y_c), JIS specified color names (hue H, value V, chroma C), and general color names are as shown.

In the general CCD shooting process, there are unit vectors of chromaticity red [R], green [G], and blue [B], which can be converted into vector operation of 3D space. This space using geometry to represent colors is known as color space, as shown in Fig. 4. Monochromatic light object stimulation $[F]_{\text{mono}}$ can be represented by the vector of RGB color space made by using mixed amounts of R, G, and B of red [R], green [G], and blue [B] as components.

The monochromatic color is usually represented by the intersection point (r, g, b) of the vector $[F]_{\text{mono}}$ and unit plan $R + G + B = 1$. The use of the left 3D space in Fig. 15 to represent $[F]$ mono-color is not convenient; thus, the $r, g,$ and b values are obtained from the following equations:

$$\begin{aligned} r &= R/(R + G + B) \\ g &= G/(R + G + B) \\ b &= B/(R + G + B) \end{aligned} \tag{3}$$

The color matching functions in the RGB apparent color system have negative values; to avoid inconvenient calculation, the XYZ apparent color system with positive tristimulus values was adopted, and the color stimulus values were [X], [Y], and [Z], also known as the CIE 1931 standard color system. When this system performs a color matching experiment, the XYZ apparent color system has a characteristic $y^-(\lambda)$, which is the same as spectral apparent efficiency. The spectral apparent efficiency uses the quantity of radiation to represent the concept of changing the spectral distribution of color stimulus into photometric quantity, suggesting that the tristimulus value Y is directly equal to the photometric

quantity (brightness) value. In addition, the wavelength end of $\lambda \geq 650 \text{ nm}$ is fixed at $z^-(\lambda) = 0$, and the calculated tristimulus value [Z] can be reduced.

The tristimulus values [R], [G], and [B] of RGB apparent color system and the tristimulus values [X], [Y], and [Z] of XYZ apparent color system can be interconverted, and the conversion can be calculated by a matrix expressed as:

$$\begin{bmatrix} X \\ Y \\ Z \end{bmatrix} = \begin{bmatrix} 2.7689 & 1.7517 & 1.1302 \\ 1.0000 & 4.5907 & 0.0601 \\ 0.0000 & 0.0565 & 5.5943 \end{bmatrix} \begin{bmatrix} R \\ G \\ B \end{bmatrix} \tag{4}$$

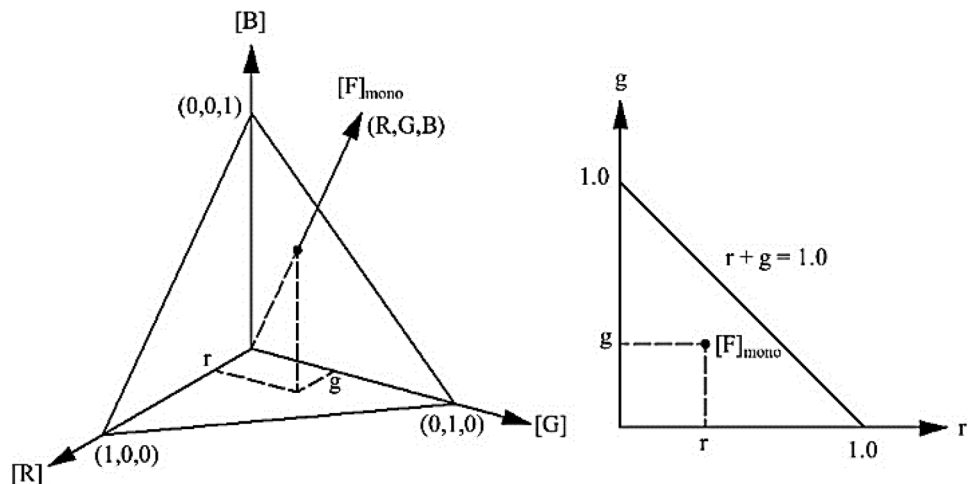
The conversion of tristimulus values [X], [Y], and [Z] into the tristimulus values [R], [G], and [B] is expressed as:

$$\begin{aligned} \begin{bmatrix} R \\ G \\ B \end{bmatrix} &= \begin{bmatrix} 2.7689 & 1.7517 & 1.1302 \\ 1.0000 & 4.5907 & 0.0601 \\ 0.0000 & 0.0565 & 5.5943 \end{bmatrix}^{-1} \begin{bmatrix} X \\ Y \\ Z \end{bmatrix} \\ &= \begin{bmatrix} 0.41844 & -0.15866 & -0.08283 \\ -0.09117 & 0.25242 & 0.01570 \\ 0.00092 & -0.00255 & 0.17858 \end{bmatrix} \begin{bmatrix} X \\ Y \\ Z \end{bmatrix} \end{aligned} \tag{5}$$

Besides the matrix operation of Eq. (5), the tristimulus values [X], [Y], and [Z] can be calculated by the following equations. Generally speaking, if the spectral distribution of color stimulus is regarded as $\varphi(\lambda)$, and color matching functions are $x^-(\lambda), y^-(\lambda),$ and $z^-(\lambda)$, the tristimulus values can be worked out by Eq. (6):

$$\begin{aligned} X &= k \int_{\text{vis}} \varphi(\lambda) \cdot x^-(\lambda) d\lambda \\ Y &= k \int_{\text{vis}} \varphi(\lambda) \cdot y^-(\lambda) d\lambda \\ Z &= k \int_{\text{vis}} \varphi(\lambda) \cdot z^-(\lambda) d\lambda \end{aligned} \tag{6}$$

Fig. 4 3D space representation and chromaticity diagram of monochromatic $[F]_{\text{mono}}$ [27]



where k is a constant.

\int_{vis} is derived from the visible light wavelength region

The tristimulus values of Eq. (7) can be changed according to different conditions. If an object is irradiated by light rays, the color stimulus of the reflected color is:

$$\varphi(\lambda) = R(\lambda) \cdot P(\lambda) \tag{7}$$

where $P(\lambda)$ is the spectral distribution of illuminating light; and then, $R(\lambda)$ is the spectral reflectivity of the reflecting object.

The color stimulus of the transmissive object is:

$$\varphi(\lambda) = T(\lambda) \cdot P(\lambda) \tag{8}$$

where $T(\lambda)$ is the spectral transmittance of the transmissive object.

Figure 4 shows that the trajectories of $\bar{x}(\lambda)$, $\bar{y}(\lambda)$, and $\bar{z}(\lambda)$ color-matching functions in XYZ apparent color system and spectrum are the same in the RGB apparent color system. When $[X]$, $[Y]$, and $[Z]$ are regarded as unit vectors, and the points of intersection with the unit plan $X + Y + Z = 1$ are defined as chromaticity coordinates, and Eq. (9) is established.

$$\begin{aligned} x &= \frac{X}{X + Y + Z} \\ y &= \frac{Y}{X + Y + Z} \end{aligned} \tag{9}$$

where x and y are chromatic values, and X , Y , and Z are tristimulus values.

Figure 5 shows the $\bar{x}(\lambda)$, $\bar{y}(\lambda)$, and $\bar{z}(\lambda)$ color matching function trajectories and spectral locus in XYZ chromaticity space, and the chromaticity coordinates of monochromatic light are called spectral chromaticity coordinates. The curve formed of chromaticity points connected according to the sequence of monochromatic light wavelength is called the spectral locus of monochromatic light, also known as a spectral locus.

If the $\bar{x}(\lambda)$, $\bar{y}(\lambda)$, and $\bar{z}(\lambda)$ color matching function trajectories are made on a 2D plane, and the maximum value and minimum value of monochromatic light wavelength in the spectral locus are connected as shown in Fig. 6, a U-shaped pattern is formed on the coordinate surface. This pattern is called XY chromaticity diagram, representing the color range the human eyes can see in nature.

The chip color measurement includes color-matching functions, tristimulus values, chromaticity diagram, and standard source, and the disparity of chromaticity diagram is further improved. For calculation, the XYZ tristimulus

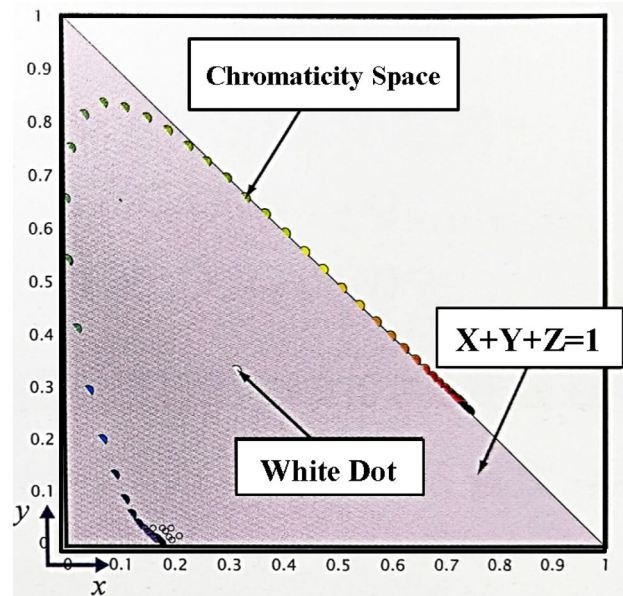


Fig. 5 Color matching function trajectory and spectral locus in XYZ chromaticity space [27]

values are substituted in $L^*a^*b^*$ and $L^*u^*v^*$ chromatic aberration modes, and the $X_{10}Y_{10}Z_{10}$ tristimulus values can be used when the observer’s viewing angle exceeds 4° .

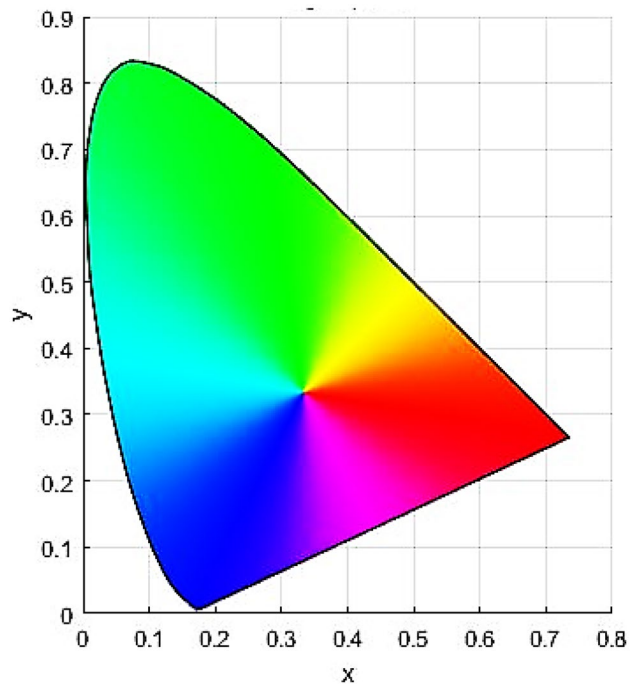


Fig. 6 CIE xy chromaticity diagram

1. The computing mode in $L^*a^*b^*$ color space is:

$$\begin{aligned}
 L^* &= 116f\left(\frac{Y}{Y_n}\right) - 16 \\
 a^* &= 500\left[f\left(\frac{X}{X_n}\right) - f\left(\frac{Y}{Y_n}\right)\right] \\
 b^* &= 500\left[f\left(\frac{Y}{Y_n}\right) - f\left(\frac{Z}{Z_n}\right)\right] \\
 f\left(\frac{I}{I_n}\right) &= \left(\frac{I}{I_n}\right)^{\frac{1}{3}}, \text{ when } \left(\frac{I}{I_n}\right) > 0.008856 \\
 f\left(\frac{I}{I_n}\right) &= 7.787\left(\frac{I}{I_n}\right) + \frac{16}{116}, \text{ and } \left(\frac{I}{I_n}\right) \leq 0.008856
 \end{aligned}
 \tag{10}$$

where $I/I_n = X/X_n = Y/Y_n = Z/Z_n$.

X , Y , and Z are tristimulus values of the object, and X_n , Y_n , and Z_n are tristimulus values of reference white. The tristimulus values vary with heterogeneous light sources if D_{50} light source of $X_n = 96.42$, $Y_n = 100$, and $Z_n = 82.49$ is used.

2. The main computing mode in $L^*u^*v^*$ color space is:

$$\begin{aligned}
 L^* &= 116f\left(\frac{Y}{Y_n}\right) - 16 \\
 u^* &= 13L^*(u' - u'_n) \\
 v^* &= 13L^*(v' - v'_n)
 \end{aligned}
 \tag{11}$$

where Y is tristimulus value Y ;

u' and v' are u and v chromaticity coordinate values of $u'v'$ chromaticity diagram; Y_n is the tristimulus value Y of reference white; and u'_n, v'_n are the chromaticity coordinate values of perfect diffusion reflection surface.

The CIE LAB and CIE LUV color spaces are specialized in representing chromatic aberration, and their color difference is worked out by the following equation. The chromatic aberration ΔE_{ab}^* between chromaticity points (L_1^*, a_1^*, b_1^*) and (L_2^*, a_2^*, b_2^*) in the CIE LAB color space is worked out by Eq. (12).

$$\Delta E_{ab}^* = \sqrt{\left[(L_1^* - L_2^*)^2 + (a_1^* - a_2^*)^2 + (b_1^* - b_2^*)^2\right]}
 \tag{12}$$

The chromatic aberration ΔE_{uv}^* between chromaticity points (L_1^*, u_1^*, v_1^*) and (L_2^*, u_2^*, v_2^*) in the CIE LUV color space is worked out by Eq. (13).

$$\Delta E_{uv}^* = \sqrt{\left[(L_1^* - L_2^*)^2 + (u_1^* - u_2^*)^2 + (v_1^* - v_2^*)^2\right]}
 \tag{13}$$

In different brightness conditions, the display shows different red, green, and blue tone scales, and the relationship between brightness and tone scale is called tone, which is usually described by the γ curve, tone reproduction curve (TRC), and photovoltaic conversion function. It is generally represented as the tone relationship between display input signal value and luminance in the display industry. The TRC of ascending tone scale signal strength and luminance of RGB primary colors of an LCD panel. The signal strength and luminance of LCD can be expressed as:

$$Y = X^\gamma
 \tag{14}$$

where X is the color signal quantity; Y is the luminous intensity; γ is the tone index (range is $1.8 \leq \gamma \leq 2.4$).

3 Experimental equipment and process

This experiment aimed to create three cutting types in different cutting parameter conditions, which are heavy cutting (Hc), medium cutting (Mc), and small cutting (Sc), and the major parameters are listed in Table 1. The experimental equipment used in this study was a CNC vertical milling machine, the five-axis machine center that the X , Y , and Z , moved on to travel 450 mm, 300 mm, and 360 mm, respectively. The feed velocity was from 36,000 to 48,000 mm/min, and the maximum revolution of the main spindle was 10,000 rpm, as shown in Fig. 7. The relationship between tool wear and experimental chips was examined, the cutting type was identified by CNN, and then the relationship of tool

Table 1 Machining experiment parameters

Cutting type	Heavy-Cutting (HC)	Medium-Cutting (MC)	Small-Cutting (SC)
Workpiece material	Nickel alloy Inconel-718		
Cutting tool adoption	SECO XOMX180631TR-ME13 F40M (insert)		
Cutting speed (m/min)	35	37	39
Feed per tooth (mm/tooth)	0.30	0.25	0.20
Depth of cut (mm)	0.40	0.25	0.1
Cutting direction	Down milling		
Cutting fluid	Dry milling		
Cutting power (kw)	0.0195	0.0107	0.0036

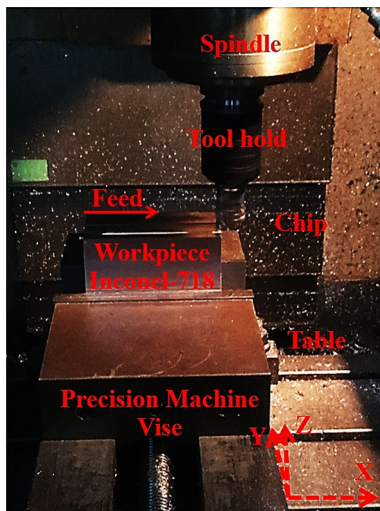


Fig. 7 The experimental equipment

wear was determined according to the xy chromatic values of chips, chip thickness, and chip width. Finally, a method for identifying the cutting type and predicting tool wear was established. The description was divided into three parts. First, the nickel alloy Inconel 718, a common alloy of the aerospace industry, was adopted for the cutting experiment. The material chips of each cutting were collected during the experimental process, the chips were photographed by industrial camera CCD, and the cutting tool wear value was measured. Second, in the process from the beginning to the intense wear of cutting tools, the pictures of chips collected in the experiment were analyzed by a human-machine interface system, and the color information xy chromatic values of chip surface were obtained. The variation trend of chip surface color xy feature values in the process from the beginning to the intense wear of the cutting tool was obtained, and the relationship between corresponding variation trends was

established. Third, the deep learning analysis and validation were performed by using the software. The pictures of material chips collected in the experiment were processed by the training networks of GoogLeNet and ResNet50 to train the convolutional neural network to identify the tool wear class, with the three types of Hc, Mc, and Sc. A cutting-type recognition model was then built by the neural network training. Finally, this recognition model was validated to obtain a confusion matrix to confirm that the capability of the recognition model has adequate accuracy, and this recognition system was completed at this time. Then, three types of tool life models were built by using BP. To further increase the model reliability, a single feature was compared with multiple fusion features in the course of modeling. To cut the hard-to-cut material nickel alloy Inconel 718 in the future, as long as the chips are photographed and the picture is input into the recognition model, the cutting type can be obtained and the corresponding BP model was selected to subsequently obtain the tool wear. A simple and rapid cutting tool wear model is provided for the industry, and the experimental process is shown in Fig. 8. The experimental plans and processes at various stages are described below.

4 Results and discussion

4.1 Experimental results of the influence of different cutting types on chip features

In the suggested conditions of this experiment, the selected experimental parameters are $V_c = 37$ m/min, $f_t = 0.25$ mm/tooth, and $a_p = 0.25$ mm. As these parameters are the median of the suggested cutting conditions, this is defined as Mc cutting type. For good experimental repeatability, three repeated experiments were performed, and the total cutting time of the cutting tool was 55.459

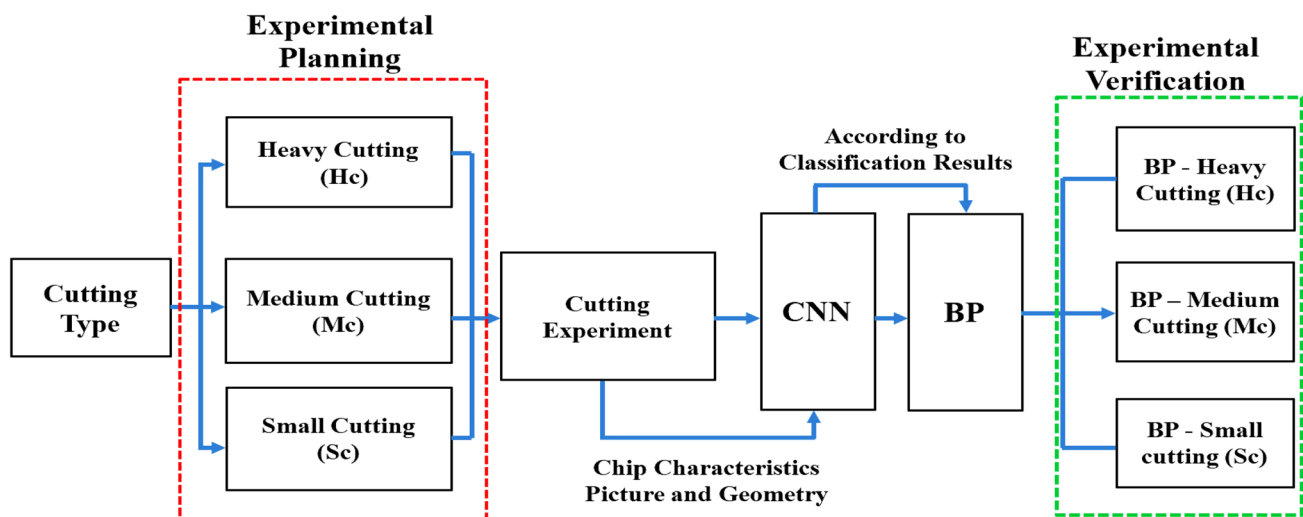


Fig. 8 A chart describing the experimental process

(min) and 60.826 (min). Each group performed 31, 34, and 34 pass cutting experiments, respectively, and stopped when the wear was 0.309 mm, 0.315 mm, and 0.351 mm, respectively. In this experiment, the correlation between tool wear and tool appearance of 1, 17, 31, and 34 cutting times was observed and represented by tool life Taylor’s curve, as shown in Fig. 9. In the repeated experiment, the maximum error was 55.54%, and the least error was 1.34%; this was for 31 and 34 passes of cutting, and the missing three passes were represented by 0. In terms of the overall mean error, the mean error of the 31st pass was 4.56%, and the mean error of the 34th pass was 9.05%.

In the suggested cutting conditions, the selected experimental parameters are $V_c = 39$ m/min, $f_t = 0.2$ mm/tooth,

and $a_p = 0.1$ mm, which are the small values in the suggested cutting conditions; hence, this is defined as the Sc cutting type. The total cutting time of the cutting tool was 150.875 (min), and there were 71 passes in the cutting experiment, which stopped when the wear was 0.306 mm. In this experiment, the correlation between tool wear and tool appearance of 1, 35, and 71 cutting times was discussed and illustrated by tool life Taylor’s curve, in Fig. 10.

As the factors influencing tool life are cutting speed, feed rate, depth of cut, and cutting width in the machining experiments, the influence of different machining conditions on the feature of chip formation was studied in this research. The parameter settings of different cutting types were categorized into Hc, Mc, and Sc cutting types

Fig. 9 Mc experiment and repeatability comparison

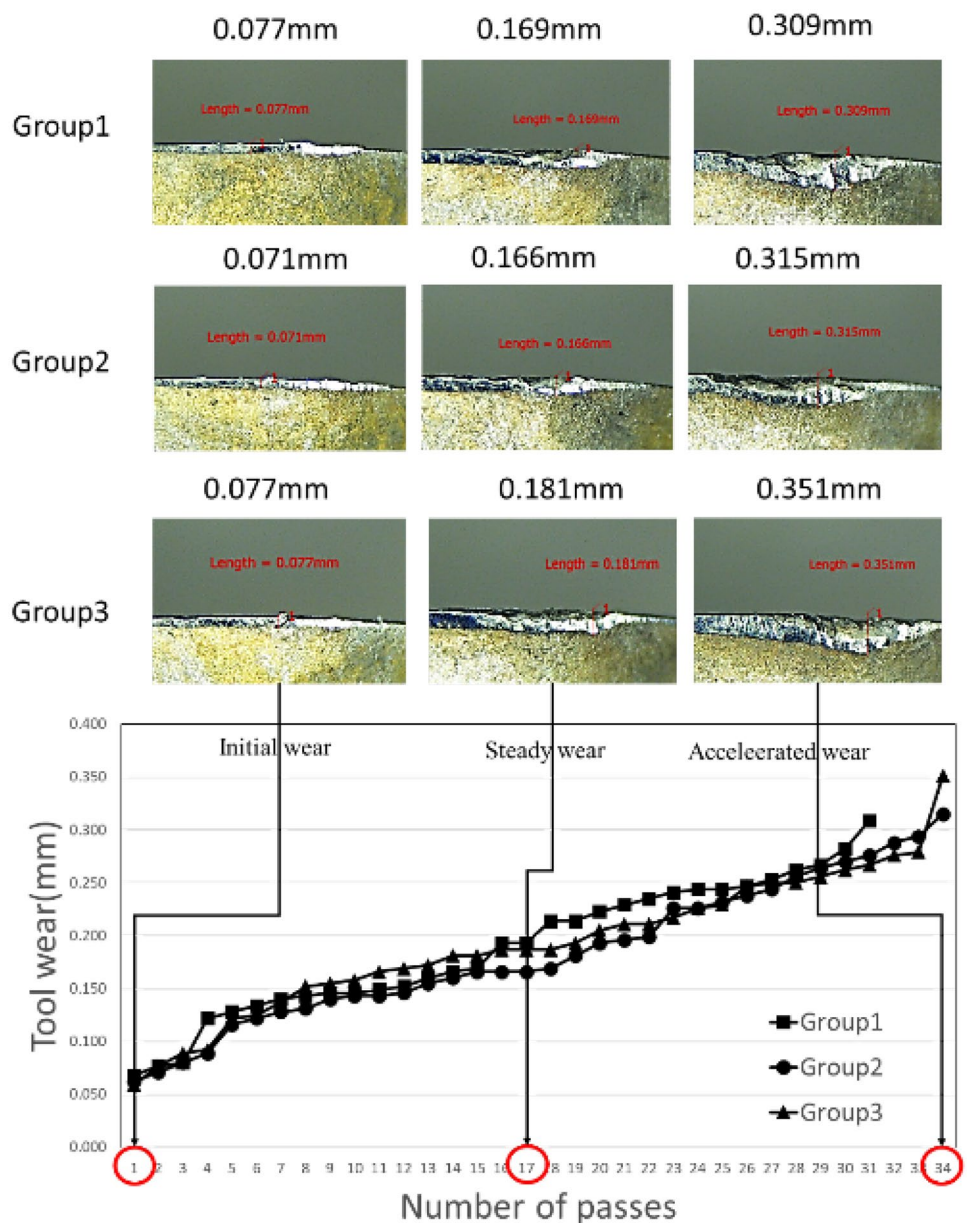
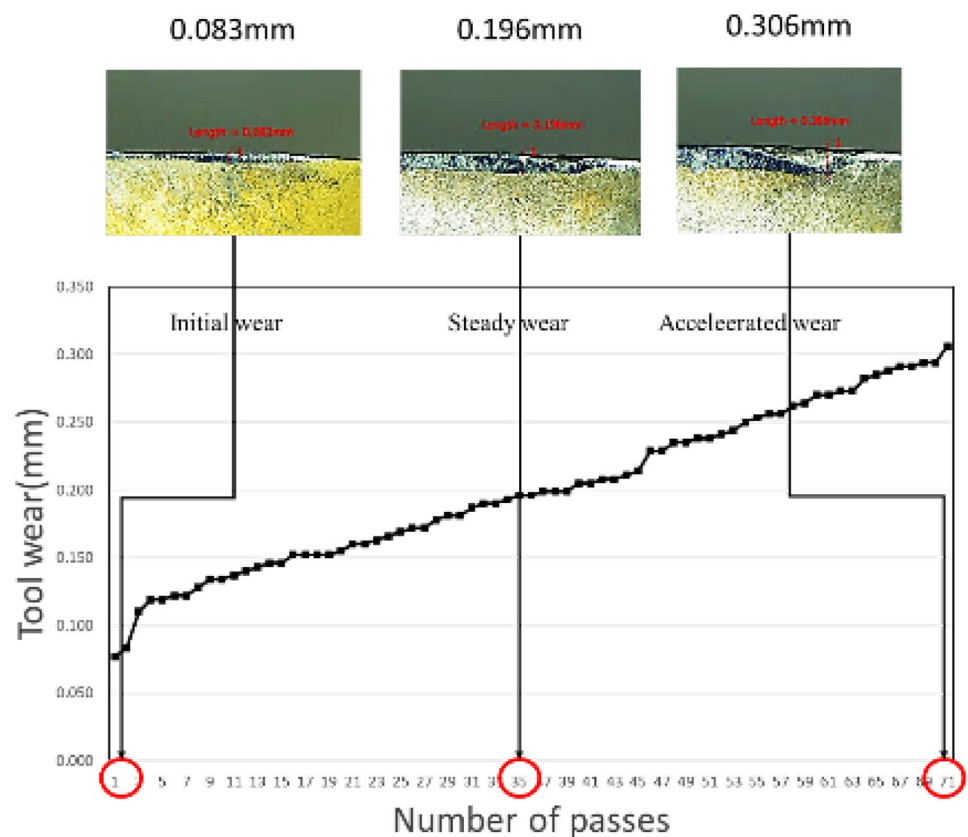


Fig. 10 Sc experiment result



according to the suggested parameters provided by the cutting tool supplier, and the detailed cutting conditions are shown in Table 1. The chips were collected in the machining experiments, and the chip features (width, thickness) in different conditions were measured by CCD industrial camera. The effects of tool wear on the chip features of Hc, Mc, and Sc in the same cutting condition are compared below with illustrations of their correlation.

In the Hc, Mc, and Sc machining experiments, the correlation of anterior, intermediate, and posterior stages of wear was discussed only. For Hc, (1, 10, 20) passes were sampled; for Mc, (1, 17, 34) passes were sampled; for Sc, (1, 35, 71) passes were sampled, as shown in Figs. 11 and 12. As the tool wear increased, the chip width in the Hc condition decreased from 1.5172 to 1.3333 mm, and the chip thickness increased from 0.1839 to 0.2011 mm. In the Mc condition, the chip width decreased from 1.1666 to 1.0862 mm, and the chip thickness increased from 0.1264 to 0.1350 mm. In the Sc condition, the chip width decreased from 0.7643 to 0.6379 mm, and the chip thickness increased from 0.0862 to 0.1034 mm. The trend of variation of an increase in chip thickness and a decrease in chip width were observed in the three experiments.

The above experimental results showed the variation of chip features (width, thickness) as the tool wear increased in

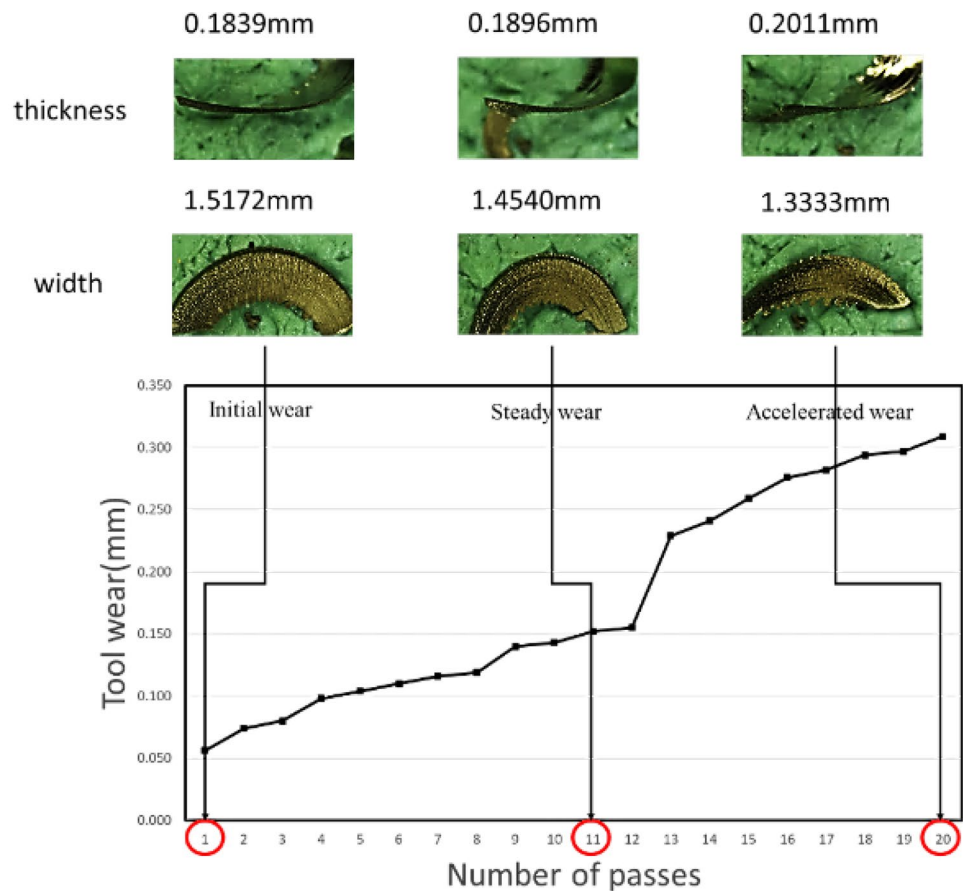
the condition of a single type. The chip thickness increased with tool wear, and they were proportional to each other. In terms of chip width, the trend was reversed with an inversely proportional relation. Then, the relationships between the three cutting types and the chip features (chip thickness and chip width) were compared. The overall chip features decreased with cutting type. The chip width and thickness are shown in Figs. 13 and 14, respectively.

In the single-type cutting conditions, the chip width decreased as the tool wear increased and the chip thickness increased. This phenomenon matches with the tool life model proposed by Swedish Prof. Bertil Colding in the 1950s. The decrease in chip thickness will increase the tool life, and an increase in cutting speed will reduce chip thickness; these phenomena also corroborate with the experimental results of our research [28].

4.2 Shooting analysis results of chip surface chromaticity of different cutting types

This section describes the results of the CIE xy chromaticity coordinate value shooting of machining chips of different cutting types. Isometric sampling was performed according to different cutting types and the number of passes in machining experiments. Ten chips were taken from each

Fig. 11 Influence of Hc tool wear on chip features



group; 90 pieces of data from nine groups were sampled from Hc, 150 pieces of data from 15 groups were sampled from Mc, and 210 pieces of data from 21 groups were sampled from Sc. A total of 450 chromaticity coordinate values were analyzed by a human–machine interface system. The CIE xy chromaticity coordinate values of chips were obtained, and the influence of tool wear in various stages of initial wear, steady wear, and accelerated wear on chip CIE xy chromaticity coordinate value was discussed. The chip CIE xy chromaticity coordinate values of three cutting types are compared in Figs. 15 and 16.

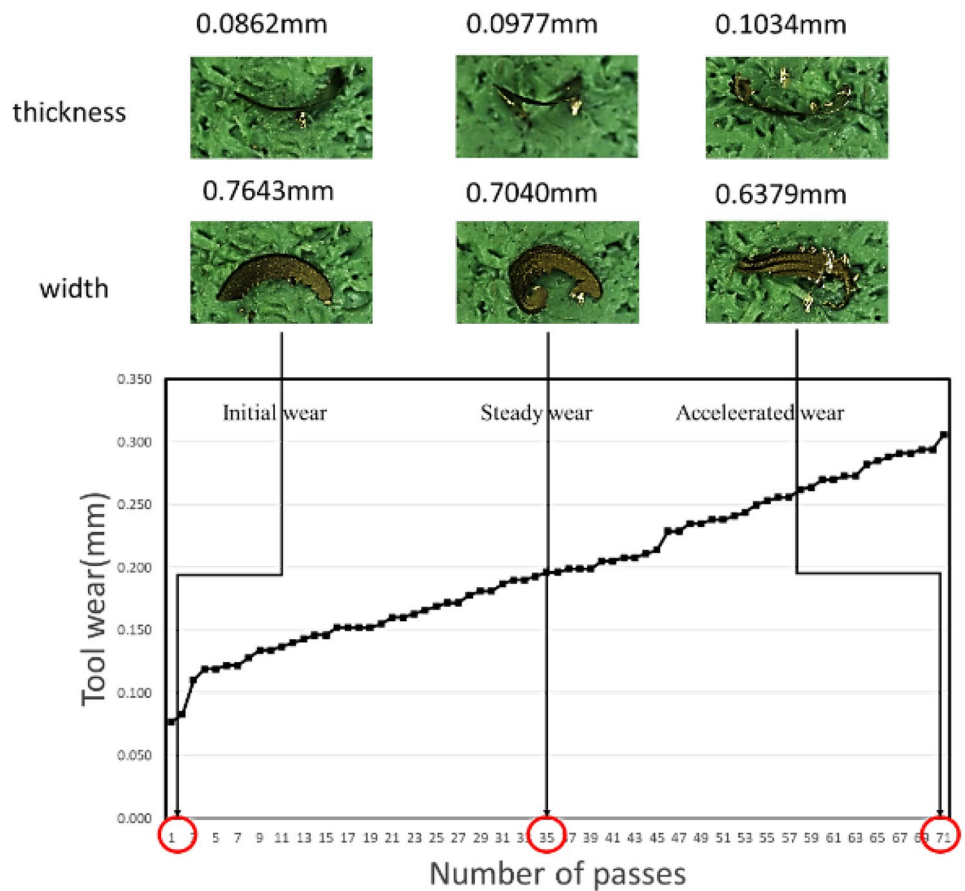
Three phenomena were obtained from the analysis results of three machining experiments. According to the relationship of different cutting types and tool wear to chromaticity surface coordinates, first, the trend in the diagram was observed, and the chromaticity coordinates xy values increased gradually with the cutting tool wear loss, which diffused towards the upper right gradually in the color horse-shoe diagram. The three cutting types matched this variation trend. Second, when the cutting tool turned from the initial unworn state into the accelerated wear state, the color trend of chip surface chromaticity eigenvalue changed from yellow to yellow–brown. Third, the chromaticity coordinate feature xy values were relatively staggered in the initial wear and

steady wear intervals, but as the tool wear entered the accelerated interval, the values changed from approximate interlacing into diffusion to separation. The said three changes might have resulted from the cutting heat generated during the cutting processes as the tool wear increased. The chips were heated up rapidly by the cutting heat and cooled rapidly in the air. This phenomenon resulted in the formation of oxidation film of different thicknesses on the surface of chips and also influenced the chromaticity coordinate xy values.

4.3 Application of CNN to recognition of different cutting types

The CNN was employed to identify different cutting types as the training samples in this study met the characteristics of transfer learning with a short training time, low hardware requirement, and limited data to achieve the optimum research benefit. However, transfer learning has to overcome the uncertainties of training accuracy and generalization ability, and these problems were overcome by using data enhancement in this study. Several different images were generated by scaling, rotation, and overturn, and the fixed light condition (angle and brightness) and shooting environment were normalized at the original image end

Fig. 12 Influence of Sc tool wear on chip features



to improve the environmental factors of image noise and reflection resulting from light change as the camera lens was capturing images and to increase the recognition rate. Four hundred and fifty original image samples were obtained after the said experiment, and the images were expanded by data enhancement, which were used as CNN modeling training samples, with 70% for training and 30% for validation. The GoogLeNet and ResNet50 network architectures were adopted for experiments and analysis, and the results are discussed below [29, 30].

In model validation, this study employed a confusion matrix to evaluate the result of the model, and the multi-classification prediction was implemented. The fundamental purpose was to visually identify the validation results of GoogLeNet and ResNet50 networks through a confusion matrix to observe the distribution of different classes. In the program part, the classify function was adopted for classification. The classify function was divided into two parts, the adopted sorting network model, and the picture data to be predicted, the confusion matrix. The row item corresponds

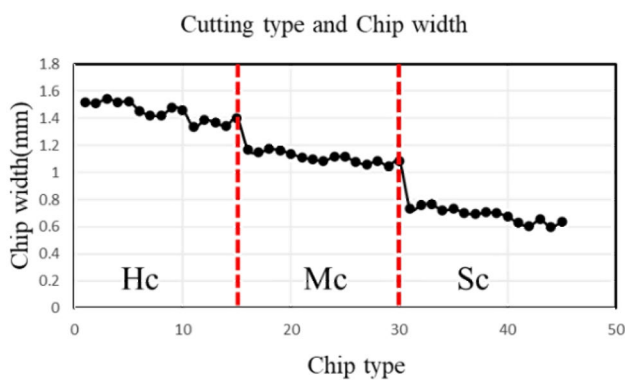


Fig. 13 Relationship between cutting type and chip width

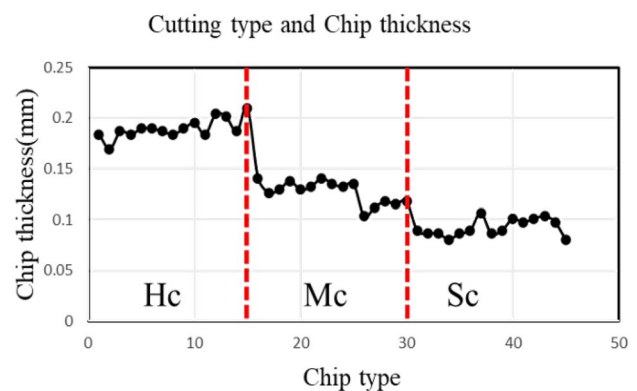
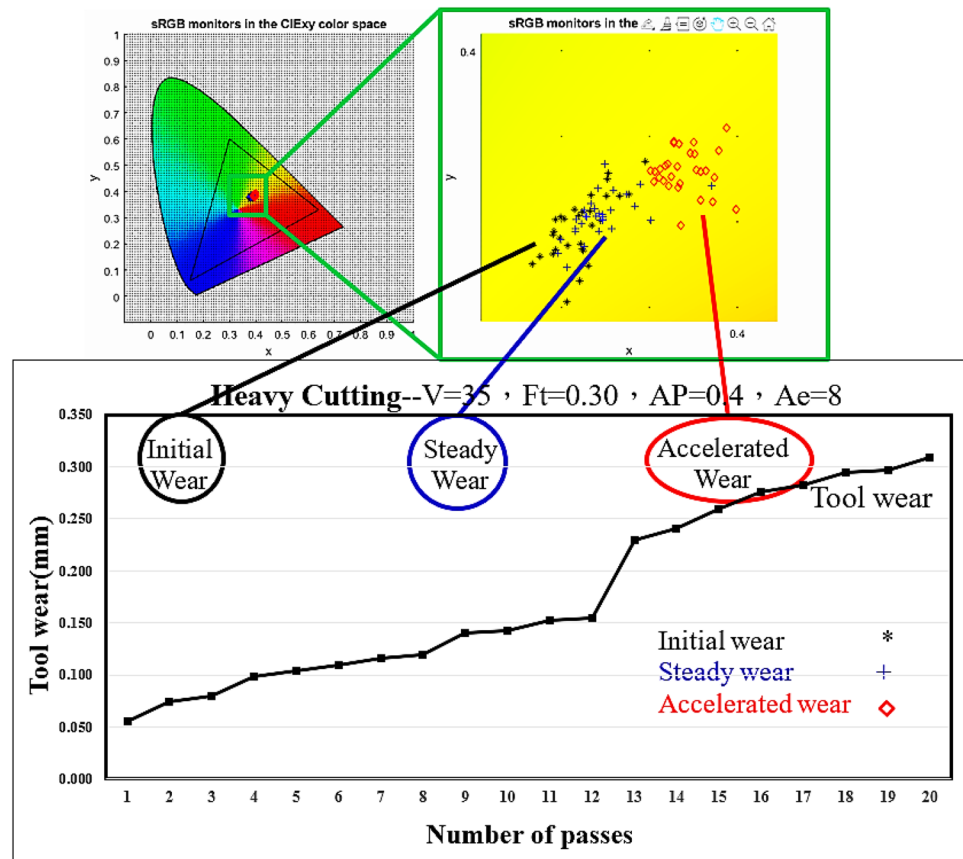


Fig. 14 Relationship between cutting type and chip thickness

Fig. 15 The relationship between Hc material chips and tool wear



to the prediction class (output class), and the column item corresponds to the reality class (target class). Each red box indicates the sample quantity of incorrect prediction, with the diagonal green box representing the number of samples of correct prediction and the light gray box representing the corresponding sample attribute prediction accuracy. The right index generally represents accuracy or positive prediction value and error discovery rate, and the lower index generally represents recall or true positive rate and false-negative rate. The computing mode is shown in Table 2 and expressed from Eqs. (15) to (17).

$$\text{Accuracy} = \frac{a + e + i}{a + b + c + d + e + f + g + h + i} \tag{15}$$

$$\text{Average Precision} = \frac{\frac{a}{a+b+c} + \frac{e}{d+e+f} + \frac{i}{g+h+i}}{3} \tag{16}$$

$$\text{Average Recall} = \frac{\frac{a}{a+d+g} + \frac{e}{b+e+h} + \frac{i}{c+f+i}}{3} \tag{17}$$

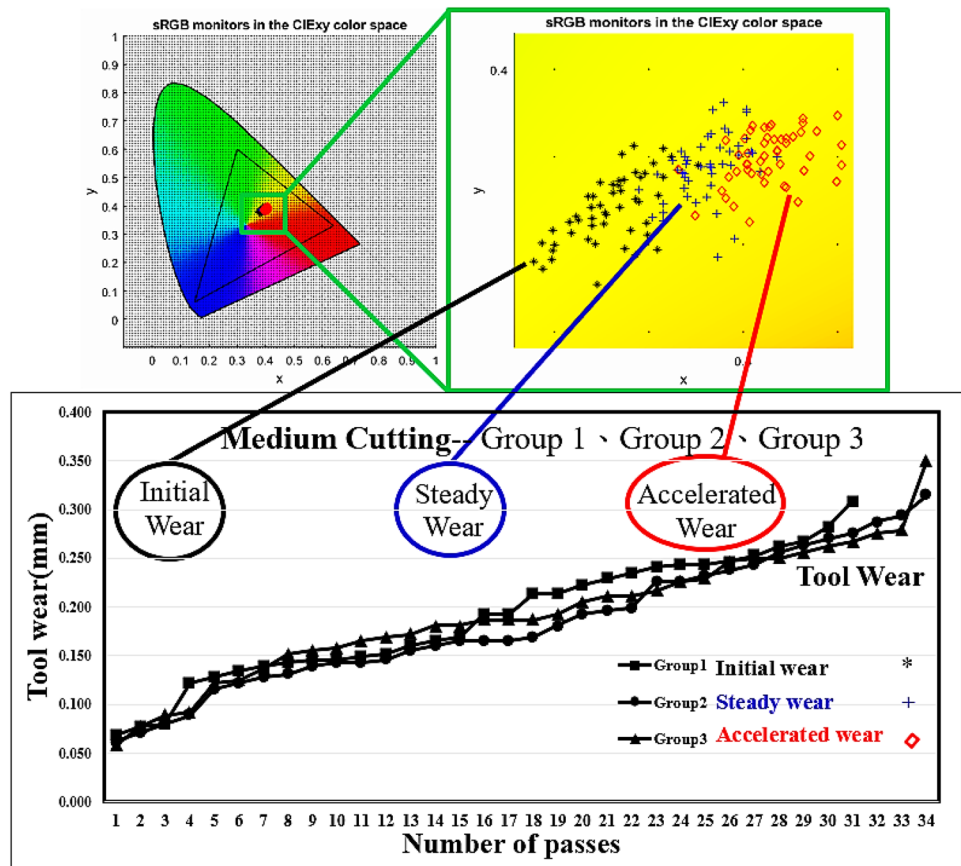
Generally speaking, 66.7% of predictions of GoogLeNet confusion matrix are correct, and 33.3% are incorrect, whereas 88.9% of predictions of the ResNet50 confusion

matrix are correct, and 11.1% are incorrect, as shown in Figs. 17 and 18. To fully evaluate the effectiveness of the model, the accuracy, average precision, and average recall of the model were compared, as shown in Table 3. ResNet50 was observed to be better than GoogLeNet in all respects; this might be because of the residual network design proposed by ResNet50. With the named design solve gradient vanishing and network deepening training degradation, the residual design removes the same principal part, highlighting subtle changes, and achieving higher accuracy. This part of the character matches the images used in this study.

4.4 Test results of tool wear prediction model of different cutting types

According to the recognition result of different cutting types of CNN in the said experiment, the cutting type could be effectively classified into Hc, Mc, and Sc types. The correlation of chromaticity coordinate value (CIE xy), chip width (width), and chip thickness (thickness) eigen factors of tool wear are known, and the chromaticity coordinate value, chip width, and chip thickness are influenced by the parameter conditions of different cutting types. Therefore, the chromaticity coordinate value,

Fig. 16 The relationship between Mc material chips and tool wear



chip width, and chip thickness were employed as feature values for tool wear modeling, providing a reference for and applications on tool life systems. The models were built according to the classification result of CNN, the prediction process is shown in Fig. 19. The experimental model is shown in Fig. 20.

Therefore, this stage aimed to obtain experimental data of three cutting types from pre-machining experiments. With the chromaticity coordinate value (CIE xy), chip width (width), and chip thickness (thickness) being the input layer, and the tool wear being the output layer, 90 data were sampled from Hc, 150 were from Mc, and 210 were from Sc, with 70% of total data being taken as training files (63, 105, and 147 data) and 30% being taken as test files (27, 45, and 63 data). Based on the assessment criteria of Lewis (1982) and Makridakis (1993), this study was further used

for training and test data collocation and adopted the mean absolute percentage error (MAPE) as the measurement index [31–34].

Table 2 Multi-classification confusion matrix

	1	2	3	Precision
1	a	b	c	$\frac{a}{a+b+c}$
2	d	e	f	$\frac{e}{d+e+f}$
3	g	h	i	$\frac{i}{g+h+i}$
Recall	$\frac{a}{a+d+g}$	$\frac{e}{b+e+h}$	$\frac{i}{c+f+i}$	$\frac{a+e+i}{a+\dots+i}$

Confusion Matrix

	1	2	3	
1	20 44.4%	10 22.2%	2 4.4%	62.5% 37.5%
2	1 2.2%	4 8.9%	1 2.2%	66.7% 33.3%
3	0 0.0%	1 2.2%	6 13.3%	85.7% 14.3%
	95.2% 4.8%	26.7% 73.3%	66.7% 33.3%	66.7% 33.3%
	1	2	3	

Fig. 17 GoogLeNet confusion matrix

Confusion Matrix

Output Class	1	2	3	
	1	2	3	95.5% 4.5%
	2	2	2	85.7% 14.3%
	3	2	7	77.8% 22.2%
	1	2	3	88.9% 11.1%
	Target Class			

Fig. 18 ResNet50 confusion matrix

In the first part of the cutting validation experiment, the model of the Hc type was built. Employing chip chromaticity coordinate value and chip thickness, chip chromaticity coordinate value and chip width, chip chromaticity coordinate value, and chip width and chip thickness; the MAPE values were 23.14%, 23.50%, and 17.11%, respectively. The model of Mc type was built in the second part, and the MAPE values were 6.74%, 9.80%, and 5.45%, respectively. The model of Sc type was built in the third part, and the MAPE values were 11.12%, 13.21%, and 9.02%, respectively. The prediction values of machining experiments and the measured cutting tool wear values are presented from Figs. 21, 22, and 23.

The tool wear prediction error percentages of model heavy, medium, and small cutting were 17.11%, 5.45%, and 9.02%, respectively. The increase of training files caused decreasing tool wear prediction error percentages and vice versa. Furthermore, it was apparent that specimen chip color + thickness + width provided better results than specimen chip color + width and chip color + width.

According to the experimental results, the prediction result of Hc was relatively high because the rate of change

Table 3 Compare ResNet50 with Google-Net

	GoogLeNet	ResNet 50
Accuracy(%)	66.7	88.9
Average precision (%)	71.63	86.33
Average recall (%)	62.87	85.93

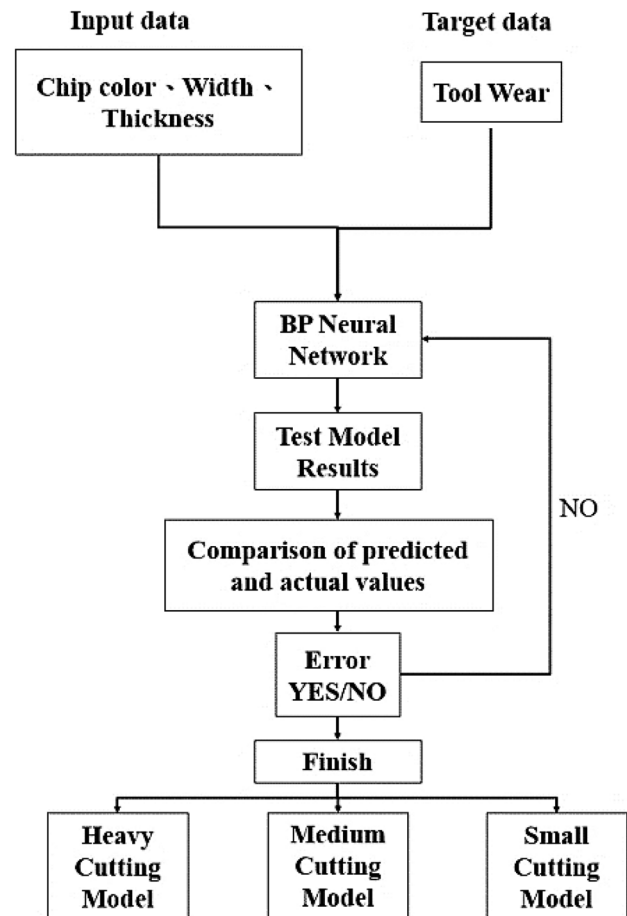


Fig. 19 Prediction modeling process

in the tool wear was higher than the other two types during cutting, the cutting stroke was shorter, and there were fewer sampled data. This led to drastic changes in values and larger errors. Generally speaking, the model has a good predictive ability, and the MAPE values of chip thickness and chip width are higher in a single condition. After the three features were fused, the MAPE value could predict the tool wear more accurately than a single feature value, and the results are shown in Table 4. This phenomenon matches with the results of Xiao yuan Wang, Chen Tong, and Xiang eng Fan in 2020 and 2021, which stated that the precision can be increased effectively by fusing multiple features [35–37].

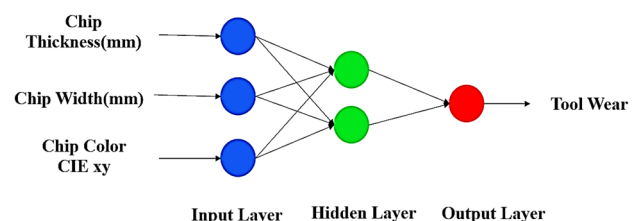


Fig. 20 Experimental model

Fig. 21 Hc tool wear prediction result

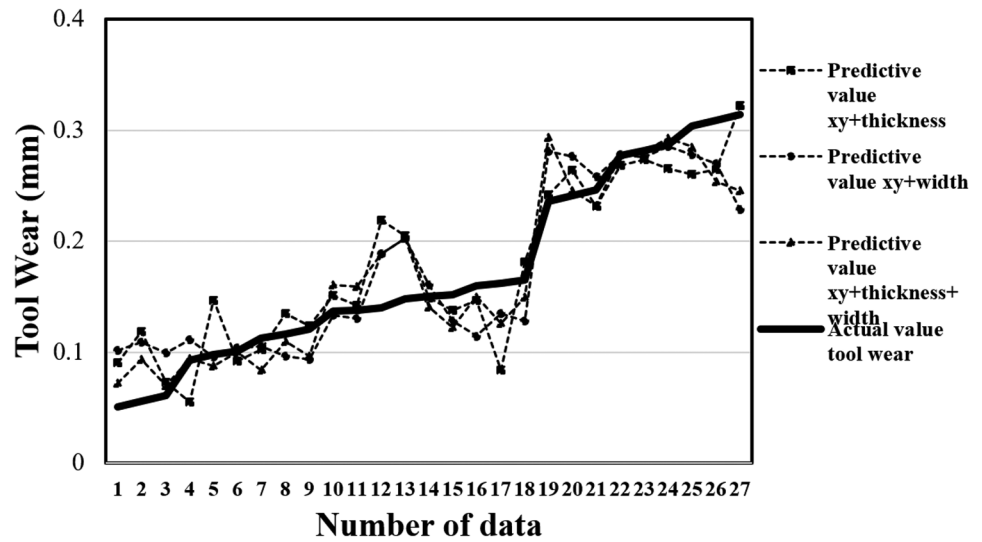


Fig. 22 Mc tool wear prediction result

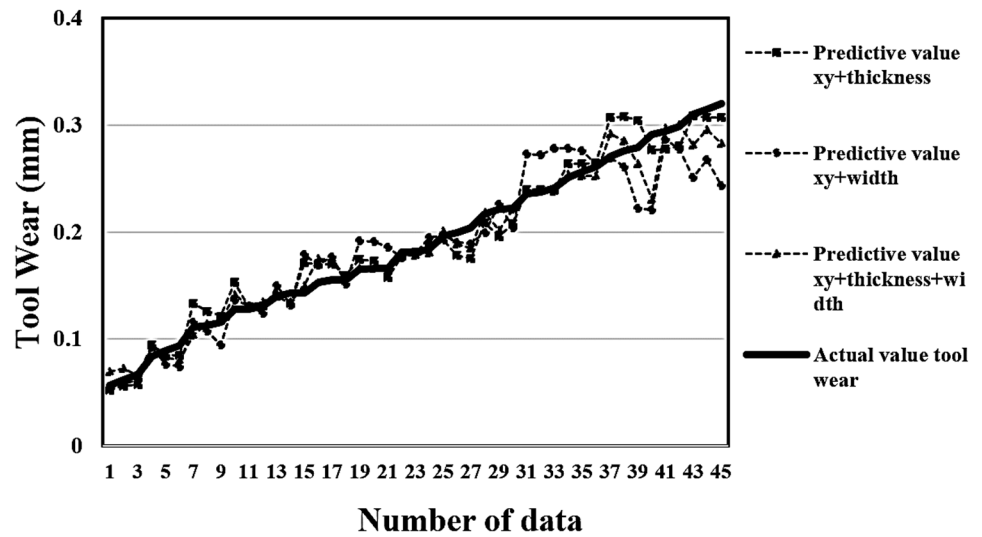


Fig. 23 Sc tool wear prediction result

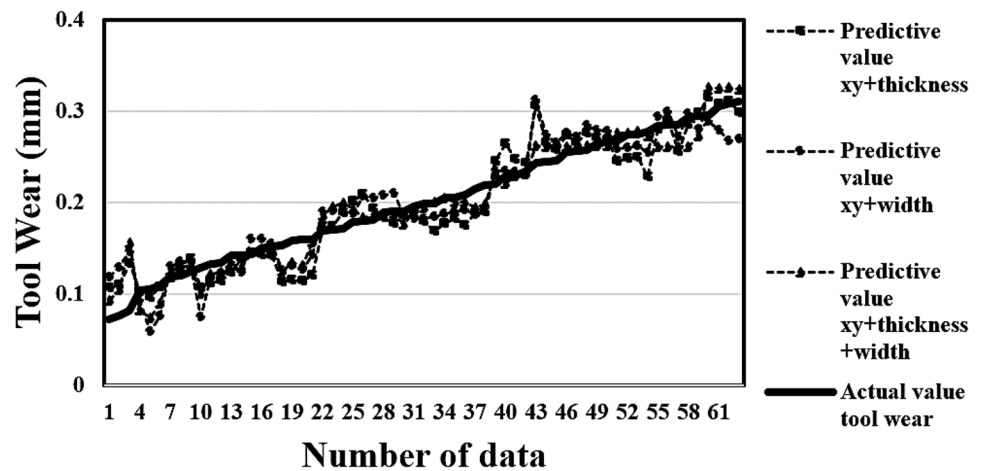


Table 4 Tool wear prediction error percentages of heavy, medium, and small cutting in BP prediction model

BP Method prediction tool wear — MAPE(%)			
Type	Heavy cutting	Medium cutting	Small cutting
Chip color x - y + thickness	23.14%	6.74%	11.12%
Chip color x - y + width	23.50%	9.80%	13.21%
Chip color x - y + thickness + width	17.11%	5.45%	9.02%

5 Conclusions and future studies

5.1 Conclusions

This study employed a hard-to-cut material nickel alloy Inconel-718 to perform dry machining experiments in different machining conditions and fused chip features for direct measurements to discuss the correlation between hard-to-cut material nickel alloy Inconel-718 and tool wear. Then, the chips and cutting tool conditions in the dry machining were observed to obtain multiple information in relation to tool wear, and the information effectively reflected the tool wear selected by data classification. The CNN GoogLeNet and ResNet 50 were adopted for classifying Hc, Mc, and Sc in different machining conditions. Finally, the modeling of tool wear was performed by using BP neural network with the chip features (cutting width, chip thickness, and CIE xy) collected in the machining experiments, and the influence of different feature input values on the measured tool wear value and predicted tool wear value was discussed. Thus, the tool wear prediction can be implemented with a certain precision, and the experimental results are detailed below.

1. The experiments showed that in dry milling of hard-to-cut material nickel alloy Inconel-718, three different cutting parameter conditions were formed according to the consumed power. The tool wear result of machining experiments showed Sc 71 passes, Mc 31, 34, and 34 passes, and Hc 20 passes, proving that the higher the cutting consumed power, the shorter the tool life. The cutting tool wear loss increased with feed rate, so the tool life shortened accordingly. When the small depth of cutting and low feed rate were combined with high cutting speed, the tool life was better than that of large depth of cutting, high feed rate, and low cutting speed, suggesting that the cutting speed was not an absolute influencing factor in different parameter conditions, and the overall factors should be considered.
2. The measurement result of machining chip features showed that the cutting width decreased as the tool wear increased, being inversely proportional to each other, and the cutting thickness also increased proportionally. The correlation between chip features and tool wear was thus proved.
3. The rotation between the cutting tool and workpiece material during machining generated high-speed friction, and thus, a lot of cutting heat. The material chips are heated up rapidly by the cutting heat and cooled rapidly in the air after leaving the parent material; this phenomenon results in the formation of oxidation film in different thicknesses on the surface of chips so that the chip color is changed. After analyzing the color information xy feature value through the human-machine interface system in this study, the correlation between tool wear and chip chromaticity xy feature value was determined. The color horseshoe diagram expanded outwards as the tool wear increased, the xy chromaticity feature value increased relatively, and the chip color moved towards the upper right from the yellow interval to the yellow brown interval. When the cutting tool was in the accelerated wear stage, the color change was the most apparent, and the color chip xy feature value was diffused most apparently.
4. This study adopted GoogLeNet and ResNet50 convolutional neural network architecture models to predict the cutting type. The result showed that the ResNet50 convolutional neural network architecture had better approximation capability than the GoogLeNet convolutional neural network architecture. When there were limited sampled data and unstable data, the comparison of tool wear prediction errors of overall experimental groups showed better prediction errors in the ResNet50 neural network model than in the GoogLeNet neural network model, with the recognition results of 66.7% for GoogLeNet and 88.9% for ResNet50, an increase of 22.2%.
5. The BP neural network model was employed to predict the cutting tool wear values of Hc, Mc, and Sc. The analysis result showed that when the chromaticity coordinate and chip thickness features were used as input values, the percentage errors of MAPE were 23.14%, 6.74%, and 11.12%, respectively. When the chromaticity coordinate and chip width features were adopted as input values, the percentage errors of MAPE were 23.50%, 9.80%, and 13.21%, respectively. When the chip width feature, chip thickness feature, and chromaticity coordinate feature were combined, the percentage errors of MAPE were 17.11%, 5.45%, and 9.02%, respectively.

Therefore, fusing multiple features could enhance the tool wear prediction accuracy more effectively than a single feature value.

Author contribution Shao-Hsien Chen: conceived and designed the analysis, contributed data or analysis tools, performed the analysis, wrote the paper. Ming-Jie Zhang: collected the data, contributed data or analysis tools, wrote the paper.

Data availability The data required to reproduce these findings cannot be shared at this time as the data also forms part of an ongoing study.

Code availability Not applicable.

Declarations

Ethics approval and consent to participate Not applicable.

Consent for publication Not applicable.

Conflict of interest The authors declare no competing interests.

References

- Sims CT, Stoloff NS, Hagel WC (1986) Superalloys. John Wiley and Sons, New York
- Kamdani K, Ashaary I, Hasan S, Lajis MA (2019) The effect of cutting force and tool wear in milling Inconel 718. *J Phys: Conf Ser* 1150:012046. <https://doi.org/10.1088/1742-6596/1150/1/012046>
- Pereira O, Celaya A, Urbikaín G, Rodríguez A, Asier Fernández-Valdivielso L, López N, de Lacalle, (2020) CO₂ cryogenic milling of Inconel 718: cutting forces and tool wear. *J Market Res* 9(4):8459–8468
- Parenti P, Puglielli F, Goletti M et al (2021) An experimental investigation on Inconel 718 interrupted cutting with ceramic solid end mills. *Int J Adv Manuf Technol* 117:2173–2184. <https://doi.org/10.1007/s00170-021-07148-6>
- Liu C, Wan M, Zhang W et al (2021) Chip formation mechanism of Inconel 718: a review of models and approaches. *Chin J Mech Eng* 34:34. <https://doi.org/10.1186/s10033-021-00552-9>
- Chen SH, Luo ZR (2020) Study of using cutting chip color to the tool wear prediction. *Int J Adv Manuf Technol* 109:823–839. <https://doi.org/10.1007/s00170-020-05354-2>
- Wright PK, Chow JG (1982) Deformation characteristics of nickel alloys during machining. *ASME, Journal of Engineering for Industry* 104:85–93
- Kurek J, Wiczorek G, Kruk BSM, Jegorowa A, Osowski S (2017) Transfer learning in recognition of drill wear using convolutional neural network. *International Conference on Computational Problems of Electrical Engineering (CPEE)*, pp. 1–4. <https://doi.org/10.1109/CPEE.2017.8093087>
- Marei M, Li W (2022) Cutting tool prognostics enabled by hybrid CNN-LSTM with transfer learning. *Int J Adv Manuf Technol* 118, 817–836. <https://doi.org/10.1007/s00170-021-07784-y>
- Xiao D, Huang Y, Zhao L, Qin C, Shi H, Liu C (2019) Domain adaptive motor fault diagnosis using deep transfer learning. *IEEE Access* 7:80937–80949. <https://doi.org/10.1109/ACCESS.2019.2921480>
- Wu X, Liu Y, Zhou X, Mou A (2019) Automatic identification of tool wear based on convolutional neural network in face milling process. *Sensors* 19:3817. <https://doi.org/10.3390/s19183817>
- Tran M-Q, Liu M-K, Tran Q-V (2020) Milling chatter detection using scalogram and deep convolutional neural network. *Int J Adv Manuf Technol* 107:1505–1516. <https://doi.org/10.1007/S00170-019-04807-7>
- Pagani L, Parenti P, Cataldo S et al (2020) Indirect cutting tool wear classification using deep learning and chip colour analysis. *Int J Adv Manuf Technol* 111, 1099–1114. <https://doi.org/10.1007/s00170-020-06055-6>
- Aslan A (2020) Optimization and analysis of process parameters for flank wear, cutting forces and vibration in turning of AISI 5140: a comprehensive study. *Measurement* 163:107959
- Kene AP, Choudhury SK (2019) Analytical modeling of tool health monitoring system using multiple sensor data fusion approach in hard machining. *Measurement* 145:118–129
- Kuntoğlu M, Sağlam H (2019) Investigation of progressive tool wear for determining of optimized machining parameters in turning. *Measurement* 140:427–436
- Kuntoğlu M, Sağlam H (2020) Investigation of signal behaviors for sensor fusion with tool condition monitoring system in turning. *Measurement* 108582
- Yang H-C, Tieng H, Cheng F-T (2016) Total precision inspection of machine tools with virtual metrology. *J Chin Inst Eng* 39(2):221–235
- Lee E-S, Kim J-D (2003) Plunge grinding characteristics using the current signal of spindle motor. *International Journal of Materials Processing Technology* 132:58–66
- Yang H-C, Li Y-Y, Wu M-N, Cheng F-T (2016) A hybrid tool life prediction scheme in cloud architecture, in *Proc. of 2016 IEEE International Conference on Automation Science and Engineering (CASE 2016)*, Aug. 21–24
- Mikołajczyk T, Nowicki K, Bustillo A, Pimenov DY (2018) Predicting tool life in turning operations using neural networks and image processing. *Mech Syst Signal Process* 104:503–513
- Peng R, Liu J, Fu X et al (2021) Application of machine vision method in tool wear monitoring. *Int J Adv Manuf Technol* 116:1357–1372. <https://doi.org/10.1007/s00170-021-07522-4>
- Fong KM, Wang X, Kamaruddin S, Ismadi M-Z (2021) Investigation on universal tool wear measurement technique using image-based cross-correlation analysis. *Measurement* 169:108489
- Shaw MC (2004) *Metal cutting principles*, Published July 8th, 2004 by Oxford University Press; 2 edition
- Li Jun Ze (2006) *Latest cutting tool science*. Xinwenjing Development and Publishing Co., Ltd
- Xu MJ (2001) *New cutting technology*, Fuhan Press
- Ri-Feng H (2011) *Display color engineering*. Quanhua Book Co., Ltd, New Taipei City
- Colding BN (1980) *The machining productivity mountain and its wall of optimum productivity*. Society of Manufacturing Engineers
- Rama Moorthy H, Upadhyaya V, Holla VV, Shetty SS, Tantry V (2020) CNN based Smart Surveillance System: a smart IoT application post Covid-19 Era, 2020 Fourth International Conference on I-SMAC (IoT in Social, Mobile, Analytics, and Cloud) (I-SMAC), 2020, pp. 72–77. <https://doi.org/10.1109/I-SMAC49090.2020.9243576>
- Khan RU, Zhang X, Kumar R (2019) Analysis of ResNet and GoogleNet models for malware detection. *J Comput Virol Hack Tech* 15:29–37. <https://doi.org/10.1007/s11416-018-0324-z>
- Gouarir A, Martínez-Arellano G, Terrazas G, Benardos P, Ratchev S (2018) In-process tool wear prediction system based on machine learning techniques and force analysis. *Procedia CIRP* 77:501–504

32. Terrazas G, Martínez-Arellano G, Benardos P, Ratchev S (2018) Online tool wear classification during dry machining using real time cutting force measurements and a CNN approach. *Journal of Manufacturing and Materials Processing* 2(4):72
33. Lewis CD (1982) *Industrial and business forecasting methods*, London: Butterworth's, London; Boston: Butterworth Scientific, 1982
34. Makridakis (1993) Accuracy measures: theoretical and practical concerns. *Int J Forecast* 9:527–529
35. Chen T, Yang J, (2021) A novel multi-feature fusion method in merging information of heterogenous-view data for oil painting image feature extraction and recognition. *Frontiers in Neurorobotics*, Original Research Article *Front Neurorobot*. <https://doi.org/10.3389/fnbot.2021.709043>
36. Fan XP, Zhou JP, Xu Y, Yang JJ (2021) “Corn Diseases Recognition Method Based on Multi-feature Fusion and Improved Deep Belief Network”, preprint. <https://doi.org/10.21203/rs.3.rs-295393/v2>
37. Wang XY, Guo YQ, Ban J, Xu Q, Bai CL, Liu SL (2020) Driver emotion recognition based on the fusion of multiple ECG features based on BP network and D-S evidence. *IET Intelligent Transportation System* 14. <https://doi.org/10.1049/iet-its.2019.0499>

Publisher's Note Springer Nature remains neutral with regard to jurisdictional claims in published maps and institutional affiliations.